Published work: https://doi.org/10.1109/VTC2024-Fall63153.2024.10757681

Beamforming-enhanced Conditional Handover for Air-to-Ground Communications in 6G

Stefan Neumann *, Thomas Meyerhoff†, Syed Aizaz Ali Shah *, Rainer Grünheid*, Gerhard Bauch *
*Institute of Communications, Hamburg University of Technology, Hamburg, Germany.
†Central Research and Technology, Airbus Operations GmbH, Hamburg/Munich, Germany.
Email: stefan.neumann@tuhh.de, thomas.meyerhoff@airbus.com, {aizaz.shah, gruenheid, bauch}@tuhh.de

***Abstract*—In high mobility scenarios, cell selection in preparation for handover is a non-trivial task. Particularly a user equipment (UE) installed on board a passenger aircraft faces a high handover frequency and strong interference from a terrestrial radio access network (RAN) due to the high velocities and altitude of the aircraft. Conventional reference signal received power (RSRP) measurements do not reflect the potential for interference mitigation in the aeronautical regime. Therefore, we incorporate beamforming into conditional handovers such that signal to interference power ratio (SIR) measurements are used for the cell selection in order to find a serving base station which provides the best SIR after beamforming. Link budget simulations to evaluate the proposed method are performed using real passenger aircraft flight trajectories and real world base station deployment data. The proposed method improves the link availability by 32 percentage points compared to the conventional handover procedure while decreasing the average handover interval by up to 0.6 s at the high UE velocities. We also show that a handover candidate filtering rule based on the direction of flight offers a trade-off by increasing the average handover interval by up to 2.3 s at the cost of availability.**

***Index Terms*—handover, beamforming, air to ground, 6G**

I. Introduction

Air-to-ground (ATG) communications have emerged as a promising use case for 5G and future 6G wireless communication networks accounting for the proliferation of uncrewed aerial vehicles (UAVs) and the increasing demand for connectivity on board commercial passenger aircraft [1]. With regard to the latter, ATG communications have the potential to significantly change the operation of aircraft in the future. For example, a remote operator could be connected to the cockpit to support the pilots in case of an emergency situation. However, the exchange of command and control (C2) information between an aircraft and a remote operator will be subject to high availability requirements [2]. In cases where a remote operator must assist in the landing of an aircraft, ultra-reliable low-latency communication (URLLC) may become essential.

Due to the high probability of line-of-sight (LOS) conditions between an aircraft at high altitudes and terrestrial base stations (BSs) in a RAN [3], an aerial user equipment (aUE) will be in radio range of a much larger number of BSs as compared to a terrestrial UE. This leads to strong interference on the downlink [4], [5]. An active electronically scanned array (AESA) installed at the fuselage of an aircraft, capable of beamforming and tracking BSs, can compensate for the strong path loss observed by the aUE at high altitudes and significantly mitigate the interference caused by non-serving BSs operating on the same carrier frequency [6], [7]. In [6], it was observed that the use of an AESA improves the availability but also affects the handovers (HOs) where an increase in availability comes at the cost of a increased HO frequency.

Conventional HO mechanisms, designed primarily for terrestrial networks, can fall short in meeting the stringent availability requirements of ATG communications that are associated with safety-critical applications. HOs to unsuitable BSs due to improper cell selection can lead to disruptions in connectivity. One advancement in this direction is the introduction of conditional handover (CHO) in 5G Release 16 [8]. With CHO, the core network provides a UE with a set of HO candidate BSs and configures the conditions to be evaluated by the UE to determine the next serving BS while the candidate BSs are prepared for a potential HO. In [9] the authors explored how trajectory information can enhance the CHO in the terrestrial context. The applicability of CHO for the non-terrestrial context has also been studied, e.g., in [10].

The integration of beamforming into HOs has been investigated for terrestrial users in [11], for high-speed trains in [12], and for mmWave applications in [13]. While [14] explores the use of signal-to-interference-plus-noise ratio prediction for improving HOs in cellular networks for terrestrial users, our study focuses on SIR measurements to enhance HOs in the aeronautical context. In [15], the authors considered LTE-based HOs for cellular-connected aircraft, but did not account for active beamsteering on the aUE side.

This paper follows the work presented in [6] and exploits the beamforming capabilities of an AESA in combination with the CHO process to improve the availability of ATG communications. To the best of our knowledge, the beamforming-enhanced (BFE) CHO has not yet been considered in the context of ATG communications.

II. Air to Ground Communication Model

The ATG communication model considered in this paper is depicted in Fig. 1. The model is characterized by the following:

- A terrestrial RAN consisting of BSs with down-tilted sector antennas operating on the same carrier frequencies.

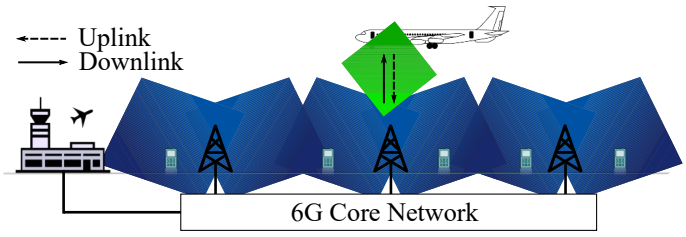

Fig. 1. ATG communications between airport and aircraft in approach in 6G

- The RAN operates in frequency division duplex (FDD) mode, which allows to consider the interference in the uplink and downlink seperately.
- An aUE installed on a passenger aircraft using an AESA mounted to the underside of the aircraft fuselage with its boresight parallel to the aircraft yaw axis.

As shown in Fig. 1, the side lobes of the down-tilted sector antennas at the BSs point towards the sky. In this work, these side lobes are used to serve aUEs at high altitudes.

For handover considerations, this study utilizes downlink measurements for RSRP and SIR. As a result, the primary metric for evaluating ATG communication is the downlink availability. The downlink is modeled using a full buffer traffic model.

Since high mobility is an inherent property of passenger aircraft, handovers occur more often in ATG communications and therefore the average handover interval (HOI) is the second relevant metric. The HOI is computed by taking the mean over the time intervals between consecutive HOs. A low average HOI, i.e., a high HO frequency, is assumed to be undesirable here. It shall be noted that the processing of HOs in the core network and the associated communication latency are not considered in the following.

The SIR observed by the aUE is obtained from the power levels of the signal emitted by a desired BS sector antenna and the interfering signals emitted by all other sector antennas of BSs in radio range. The receive power from any BS sector antenna is given by

$$P_{\mathrm{r,dBm}} = P_{\mathrm{t,dBm}} + G_{\mathrm{t,dBi}} + G_{\mathrm{r,dBi}} - L_{\mathrm{dB}} + X_{\mathrm{dB}}, \qquad (1)$$

where $P_{\mathrm{t,dBm}}$ is the BS transmit power in dBm, L_{dB} is the path loss in dB and X_{dB} is the zero-mean normal distributed shadow fading with a standard deviation σ_X.

The gain $G_{\mathrm{t,dBi}}$ of a BS sector antenna is subject to an antenna pattern with fixed directivity, while the gain $G_{\mathrm{r,dBi}}$ at the aUE depends on the beamforming applied at the AESA for connecting with the serving BS. Specifically, the beamforming at the AESA electrically steers the mainlobe towards the targeted BS. Hence, for a given aUE position and AESA beam configuration, the desired or interference power $P_{\mathrm{r,dBm}}$ determined by (1) significantly depends on the directivity of the antennas. Thus gain values depend on the azimuth and zenith angles associated with the LOS path between the AESA and the considered BS sector antenna. The antenna patterns are derived from antenna array geometries, element models, mechanical boresight directions and beam configurations.

TABLE I
σ_X AND $\hat{\sigma}_X$ FOR DIFFERENT ELEVATION ANGLES θ_{BS}

θ_{BS} in deg.	10	20	30	40	50	60	70	80	90
σ_X in dB	1.79	1.14	1.14	0.92	1.42	1.56	0.85	0.72	0.72
$\hat{\sigma}_X$ in dB	3.29	2.64	2.64	2.42	2.92	3.06	2.35	2.22	2.22

Due to the non-deterministic path loss with shadow fading, the receive power level from the BSs are treated as random variables. Consequently, the instantaneous SIR is also a random variable. Given an SIR threshold γ_{min}, we want to assess the outage probability, i.e., the probability that the SIR falls below γ_{min} at a certain trajectory point.

The interference component of the SIR in the dB scale is approximated as a normal distributed random variable using the Fenton-Wilkinson approximation [16]. Since the logarithmic receive power $P_{\mathrm{S,dBm}}$ from the serving BS is also normal distributed with mean $\bar{P}_{\mathrm{S,dBm}}$ and σ_{S} as the standard deviation from the shadow fading term, the overall SIR in dB can be approximately modeled as a normal random variable with mean $\gamma_{\mathrm{FW}} = \bar{P}_{\mathrm{S,dBm}} - \bar{P}^{\mathrm{FW}}_{\mathrm{I,dBm}}$ and standard deviation $\sigma_{\mathrm{FW}} = \sqrt{(\sigma_{\mathrm{S}})^2 + \sigma_{\mathrm{I}}^{\mathrm{FW}\ 2}}$. Here, the terms $\bar{P}^{\mathrm{FW}}_{\mathrm{I,dBm}}$ and $\sigma^{\mathrm{FW}}_{\mathrm{I}}$ are the outputs from the Fenton-Wilkinson approximation of the sum of interference powers. Given the mean γ_{FW} and standard deviation σ_{FW} of the approximate SIR distribution, the outage probability can be computed for a threshold γ_{min} as described in [16] by

$$p_{\mathrm{out}} = \frac{1}{2}\mathrm{erfc}\left(\frac{\gamma_{\mathrm{FW}} - \gamma_{\mathrm{min}}}{\sqrt{2}\sigma_{\mathrm{FW}}}\right) \qquad (2)$$

where $\mathrm{erfc}(.)$ is the complementary error function.

Finally, the availability of the link over the complete trajectory can be assessed by computing the fraction of time at which p_{out} is below a target outage probability $p^{\mathrm{th}}_{\mathrm{out}}$. A detailed walk-through from (1) to (2) can be found in [6].

For modeling path loss and shadow fading in ATG communications, we use the 3GPP model from [3]: The path loss is modeled according to free-space propagation. The shadow fading standard deviation, denoted by σ_{3GPP}, depends on the elevation angle θ_{BS} from the perspective of a BS to the aUE. Since ATG channel measurements in the literature [17], [18] have reported shadow fading with a standard deviation in the range of 2.2- 3.9dB, we use two models for the shadow fading standard deviation according to

$$\sigma_X = \sigma_{\mathrm{3GPP}} \qquad (3)$$

$$\hat{\sigma}_X = \sigma_{\mathrm{3GPP}} + 1.5\mathrm{dB} \qquad (4)$$

where $\hat{\sigma}_X$ is the same elevation angle dependent 3GPP model with a constant additive offset. The modified model accounts for the stronger shadow fading of the measurements found in literature. The exact value of σ_X and $\hat{\sigma}_X$ for a given θ_{BS} is determined by linear interpolation between the values specified in Table I.

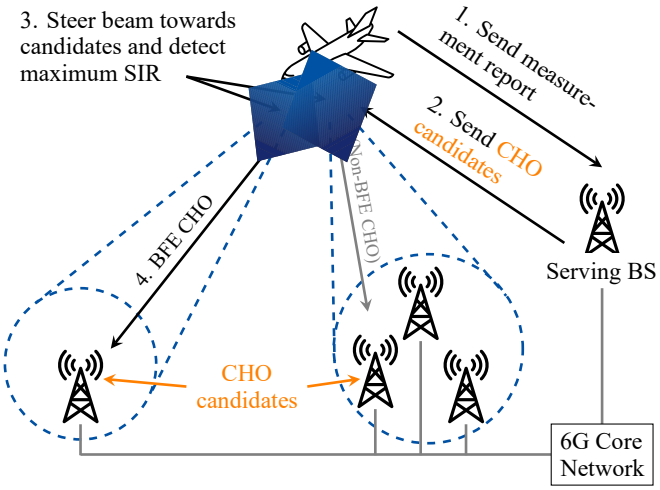

Fig. 2. Beamforming-enhanced CHO procedure

III. Beamforming -enhanced Conditional Handover

For enabling beamforming-enhanced (BFE) CHO, we assume that the aUE and core network are aware of the aircraft position and the locations of the BSs. Fig. 2 depicts the proposed BFE CHO in comparison to the conventional CHO without beamforming. The BFE CHO procedure consists of the following steps:

1) The aUE performs reference signal received power (RSRP) measurements to determine the BSs in radio range and sends these measurements to the serving BS, denoted by s, in the form of a measurement report. In our simulation we are using the received signal power P_r determined by (1) as a substitute. For this step, the AESA is configured so that it approximates an omni-directional antenna pattern as closely as possible. In this work, this is achieved by using reception from a single antenna array element.
2) Based on the measurement report, the core network determines a set of CHO candidate BSs denoted by C and signals it towards the aUE. At the same time the core network prepares the candidate BSs for a potential handover.
3) The aUE determines the azimuth and zenith angles towards all BSs in C relative to the AESA mechanical boresight and sequentially steers its main beam towards these candidates for determining the average SIRs. In this work, the average SIR γ_c observed for a given candidate BS $c \in C$ after beamforming is obtained from (1) by removing the term X_{dB} from the equation. In an operational scenario the SIR can be determined as described in [19].
4) The aUE starts the preparation of an HO to the candidate BS $s^* \in C$ that exhibits the highest SIR when the following condition is met:

$$\gamma_{s^*} > \gamma_s + \text{Handover Offset} \quad (5)$$

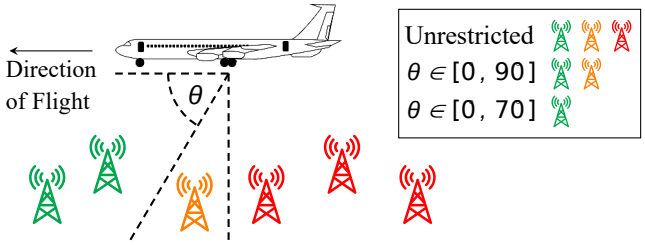

Fig. 3. CHO candidate filtering based on angle $\theta \in [0, 180]$

with

$$s^* = \arg\max_{c \in C} \gamma_c$$

where γ_s denotes the average SIR of the serving BS. The handover offset mitigates the so-called ping pong handovers [20], an undesirable effect which causes a decrease in average HOI.

To support the described procedure, we assume that the AESA is capable of forming two independent receive beams and that the aUE is able to process the two resulting signals in parallel. This allows the aUE to perform timely SIR measurements concurrently to data transmission.

After the preparation of an HO is completed, the handover target BS s^* becomes the new serving BS s which is then tracked by the AESA main lobe for communication.

The intuition behind BFE CHO can be understood by considering the impact of potentially non-serving BSs on the SIR with respect to a CHO candidate BS as depicted in Fig. 2. With beamforming towards a candidate BS during an SIR measurement, the measurement will be primarily affected by the interference of those BSs, which are illuminated by the main lobe. Hence, the combination of beamforming and SIR into the handover decision making process is supporting a candidate selection that accounts for both the desired receive signal power as well as the interference environment local to the candidate BS. Without beamforming, the possible increase in SIR offered by the AESA is not accounted for, which can lead to an HO to an unsuitable BS as shown by the grey arrow in Fig. 2.

Further improvement in terms of increasing the average HOI of the BFE CHO can be expected if the core network filters out BSs that are undesirable CHO candidates as they may move out of radio range in the near future. For this purpose, we consider two different filtering rules based on the zenith θ and azimuth ϕ angles relative to the AESA mechanical boresight as depicted in Fig. 3. The corresponding filter ensures that only BS in the angular ranges given in the figure are included in C. This type of filtering will increases the probability of an HO to a BS towards which the aircraft is moving. Such an HO is likely to result in a good SIR for a longer duration as compared to an HO to a BS that the aircraft is flying away from, yielding less frequent HOs.

IV. Simulation Setup

For evaluating the downlink availability and the average HOI, link budget simulations for three representative flight

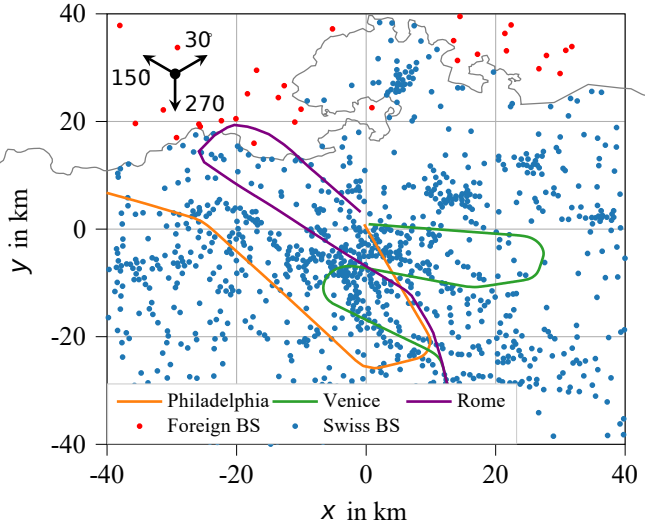

Fig. 4. Base station deployment model for urban coverage in the area around Zurich airport along with the selected flight trajectories

trajectories in approach to Zurich airport are performed. The simulations utilize 5G BS deployment data provided by the Swiss Federal Office of Communications [22] to model a realistic RAN with a dense BS deployment in a populated area. We assume that the corresponding sites will be upgraded with the transition from 5 to 6G technology and expect that the following results will also be applicable for a future 6G deployment.

The deployment model and the three flight trajectories are depicted in Fig. 4. The figure shows that the deployment model further includes BSs in neighboring countries. These foreign BSs are a source of interference and the aUE cannot connect to them. The positions of these BSs were estimated from data obtained from OpenCelliD.org.

Table II provides an overview of the simulation parameters. Similar to the AESA model used in [6], we assume a uniform planar array (UPA) with 16×16 elements to be

TABLE II
SIMULATION PARAMETERS

Parameter	Value
Carrier frequency f_c	2.14 GHz (Band n1, FDD)
Target outage probability $p_{\text{out}}^{\text{th}}$	10^{-5}
Handover offset	3 dB
RAN model	Switzerland deployment data
RAN minimum inter-site distance	500 meters
BS transmit power P_t	38 dBm
Antenna array element model	As in [21], with 8 dBi max. gain
BS antenna array model	8×1 ULA, 0.5λ element spacing
BS beamforming method	All-ones beamforming weights
BS sector antenna directions	30°, 150, 270
Mech. downtilt BS antenna array	3°
aUE AESA model	16×16 UPA, 0.5λ element spacing
aUE AESA beamforming method	Equal gain combining (Conjugate array response vector)

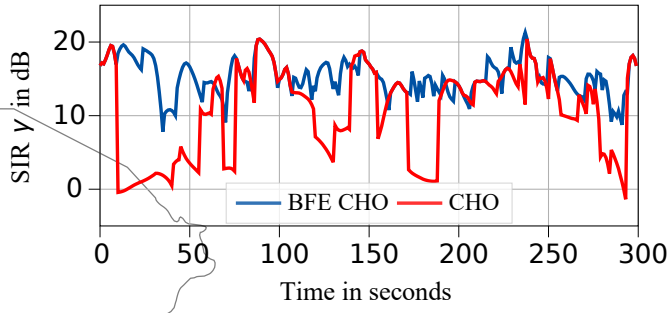

Fig. 5. SIR γ for the Venice trajectory and the BFE and conventional CHO procedures

installed on board an aircraft. The UPA has a physical size of $1.05\text{m} \times 1.05\text{m}$ for the considered carrier frequency of $f_c = 2.14\text{GHz}$ and element spacing of 0.5λ, where λ is the wavelength. The array elements are modeled as described in [21] and provide a maximum gain of 8 dBi. The beamforming method used for cell selection and data transmission is equal gain combining, which uses the conjugate array response vector in the direction of the target BS as the beamforming weights. Note that the array response vector only includes the phase differences towards each antenna element in our setup. Thus, the AESA model provides a maximum gain of $8\text{dBi} + 10\log_{10}(16^2)\text{ dBi} \approx 32\text{ dBi}$ with a 3-dB beamwidth of approximately 6.3° when the main lobe is steered to the boresight direction.

The AESA main lobe can be arbitrarily steered towards any azimuth angle $\phi \in [-90°, 90]$ and zenith angle $\theta \in [0, 180]$ in the local coordinate system of the AESA. Furthermore, the three approach trajectories are evaluated for altitudes above 300 m as serving BSs tend to move out of the scanning range of the AESA at lower altitudes.

V. Results and Discussion

In this section results regarding the availability and average HOI $\overline{T}_{\text{HO}}$ are presented for the BFE CHO and conventional CHO procedure. For computing the availability, an SIR threshold of $\gamma_{\min} = 0\text{dB}$ is used in (2) in combination with a target outage probability of $p_{\text{out}}^{\text{th}} = 10^{-5}$.

Fig. 5 depicts the average SIR γ over the first 300 s of the Venice trajectory using the CHO procedure with and without the proposed beamforming enhancement. The BFE CHO leads to a higher average γ for most of the trajectory. At certain trajectory points, e.g., at the 10 s mark, the conventional CHO leads to HOs which consequently result in γ dropping by several dB over more than 10 s w.r.t. the proposed enhancement.

For certain short parts of the trajectory (e.g., visible at 67, 144 and 197 s in Fig. 5), the conventional CHO yields higher SIR values compared to the BFE CHO. This difference results from the handover offset, which is set to 3 dB in our simulation.

For more insight Fig. 6 provides a detailed view of the handover decision at the 10 s mark. The figure shows the average SIR γ and the receive signal power P_r for three BSs relevant for the handover for both CHO types. The blue circle

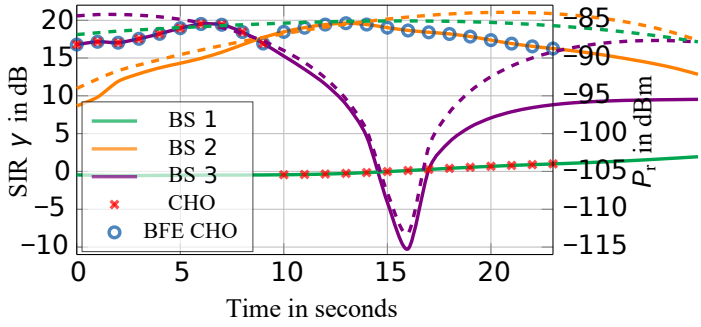

Fig. 6. SIR γ and receive power P_r for the three BSs involved in the first handover of BFE CHO and conventional CHO (solid line: γ, dashed line: P_r)

and red cross markers track γ from the serving BS with BFE and conventional CHO, respectively.

The BS 1 in Fig. 6 serves as an example of an unsuitable BS since it provides a considerably low γ for the depicted trajectory duration. Initially BS 3 provides the highest γ and P_r among the considered BSs and is chosen as the serving BS for the BFE CHO as well as the conventional CHO scenario. As the trajectory progresses, the γ and P_r of BS 3 decrease simultaneously. Beyond the 8s mark, the BS 3 no longer provides the highest γ. The 3dB handover offset prevents the handover to BS 2 until the 10s mark under the BFE CHO. Consequently, a γ over 15dB is maintained in using the proposed BFE handover as highlighted by the blue circular markers in Fig. 6.

In contrast, the conventional CHO procedure observes a higher P_r from BS 1 w.r.t the serving BS 3 at the 8s mark. The handover to BS 1 is postponed until the 10s mark due to the 3dB handover offset. Despite providing the highest P_r, BS 1 offers the lowest SIR. This behaviour is caused by high main lobe interference when steering the AESA at the aUE towards BS 1. Beginning at the 15s mark, BS 2 provides the highest P_r. However, BS 1 remains the serving BS since the difference between the P_r values from BS 1 and BS 2 does not exceed the 3dB handover offset. As a result, the conventional CHO provides a significantly low γ due to performing the last handover to an unsuitable BS.

Table III provides an overview over the simulated availabilities for the three trajectories, the different CHO types and shadow fading standard deviation models σ_X and $\hat{\sigma}_X$ as introduced in (3) and (4). For all trajectories and both standard deviation models σ_X and $\hat{\sigma}_X$, the availability over the trajectory with the BFE CHO was always at least 12.9 percentage points higher compared to the conventional CHO. It was even up to 31.42 percentage points higher for the Rome trajectory with the model $\hat{\sigma}_X$ configured. When using the σ_X model, the BFE CHO achieves availabilities above 98% on two flight trajectories. In comparison the highest availability value obtained by the conventional CHO is only around 85%.

For the considered scenarios, the average HOI is depicted in the last column of Table III. It can be observed that $\overline{T}_{HO}$ is only slightly decreased by a maximum of 0.6s over all trajectories when using the BFE CHO over the conventional

TABLE III
AVAILABILITY IN % AND $\overline{T}_{HO}$ IN SECONDS FOR $\gamma_{min} = 0$ dB FOR VARIOUS SCENARIOS

Trajectory	σ_X or $\hat{\sigma}_X$	CHO Type	Availability	$\overline{T}_{HO}$
Rome	σ_X	BFE CHO	83.18	7.3
		CHO	68.06	7.6
	$\hat{\sigma}_X$	BFE CHO	62.19	7.3
		CHO	30.77	7.6
Venice	σ_X	BFE CHO	98.08	7.3
		CHO	77.42	7.4
	$\hat{\sigma}_X$	BFE CHO	79.98	7.3
		CHO	50.91	7.4
Philadelphia	σ_X	BFE CHO	98.67	5.7
		CHO	85.73	6.3
	$\hat{\sigma}_X$	BFE CHO	89.48	5.7
		CHO	64.21	6.3

TABLE IV
AVAILABILITY IN % AND $\overline{T}_{HO}$ IN SECONDS FOR $\gamma_{min} = 0$ dB FOR DIFFERENT TYPES OF BFE CHO CANDIDATE SET FILTERING

Trajectory	Candidate Filtering	Availability	$\overline{T}_{HO}$
Rome	Unrestricted	83.18	7.3
	$\theta \in [0^\circ, 90^\circ]$	78.49	9.6
	$\theta \in [0^\circ, 70^\circ]$	73.66	10.7
Venice	Unrestricted	98.08	7.3
	$\theta \in [0^\circ, 90^\circ]$	91.59	9.0
	$\theta \in [0^\circ, 70^\circ]$	90.84	9.0
Philadelphia	Unrestricted	98.67	5.7
	$\theta \in [0^\circ, 90^\circ]$	98.43	7.3
	$\theta \in [0^\circ, 70^\circ]$	94.56	7.2

CHO. This shows that the BFE CHO procedure results in a generally higher availability at approximately the same average HOI.

Table IV shows the effect of BFE CHO candidate filtering on the availability and $\overline{T}_{HO}$ for the σ_X model. The results indicate that restrictions on the CHO candidate sets decrease the availability. Nonetheless, this decrease is less than 7 percentage points over all trajectories for the filtering type where $\theta \in [0^\circ, 90^\circ]$. At the same time $\overline{T}_{HO}$ increases by more than 1.6s over all trajectories. However, for the most restrictive case where $\theta \in [0^\circ, 70^\circ]$, this trend only holds for the Rome trajectory, whereas for the other two trajectories the availability decreases further with no improvements of the $\overline{T}_{HO}$. This shows that CHO candidate set filtering can be useful to navigate the trade-off between the average HOI and availability.

Finally, we want to assess the dependency of the availability on the SIR threshold γ_{min} as can be seen in (2). The acceptable SIR at the receiver is influenced by various parameters like the chosen modulation, coding scheme, target block error rate, etc. Therefore, Fig. 7 shows the obtained availabilities for the standard deviation model σ_X over γ_{min}. For $\gamma_{min} = -6$ dB, the conventional CHO still results in an availability that is

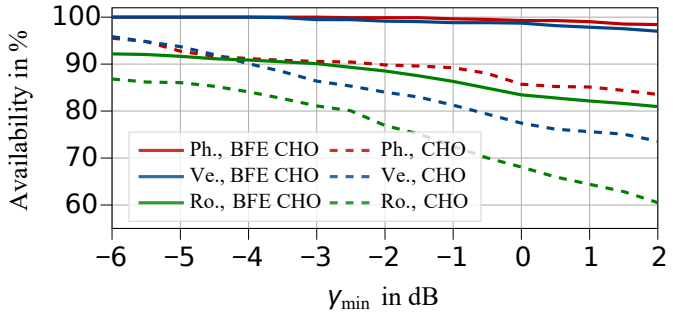

Fig. 7. Availability for BFE CHO and conventional CHO for the σ_X model

5 percentage points lower compared to our approach across all three trajectories. This gap gets larger as $\gamma_{\min}$ increases, e.g., at $\gamma_{\min} = 2$ dB, the conventional CHO leads to an availability that is 20 percentage points lower compared to our approach for the Venice and Rome trajectories. Hence, the BFE CHO procedure proposed in this paper provides a consistently higher availability than the conventional CHO procedure in the considered $\gamma_{\min}$ range.

VI. Conclusion

In this paper we proposed a modified CHO procedure for ATG communications, which leverages the use of beamforming not only during data transmission, but also during cell selection for improved handovers.

An inverse relation between availability and average HOI was observed. The simulation results suggest that the inclusion of beamforming into the CHO process can increase the SIR at the aUE significantly, yielding availabilities up to 98.7% compared to a maximum of 85.7% for the conventional CHO. This advantage was obtained consistently for different SIR threshold values $\gamma_{\min}$. At the same time the average handover intervals did not decrease by a significant amount from using the proposed method, which shows that it results in approximately equally frequent handovers compared to the conventional CHO procedure. Furthermore, we showed that the implementation of angle-based filtering rules for the CHO candidates can improve the average HOI by more than 1.6s over all considered trajectories which only resulted in slight decreases of the measured availabilities.

Future work could consider trajectory prediction for CHO for passenger aircraft to improve the CHO preparation. Other RAN deployment models, e.g., with a small number of up-tilted BS antennas to improve aerial coverage, could also be studied.

Acknowledgment

This work was supported by the German Federal Ministry of Education and Research (BMBF) project 6G-ANNA (grant agreement number 16KISK104) and Airbus.

References

[1] A. Baltaci, E. Dinc, M. Ozger, A. Alabbasi, C. Cavdar, and D. Schupke, "A Survey of Wireless Networks for Future Aerial Communications (FACOM)," *IEEE Communications Surveys & Tutorials*, vol. 23, no. 4, pp. 2833–2884, 2021.

[2] RTCA, *Minimum Aviation System Performance Standards for C2 Link Systems Supporting Operations of Unmanned Aircraft Systems in U.S. Airspace*, Radio Technical Commission for Aeronautics Std. DO-377, Mar. 2019.

[3] 3rd Generation Partnership Project (3GPP), "Air-to-ground network for NR, 3GPP TR 38.876 Version 18.0.0," Dec. 2023.

[4] ——, "Study on Enhanced LTE Support for Aerial Vehicles, 3GPP TR 36.777 Version 15.0.0," Dec. 2017.

[5] I. Kovacs, R. Amorim, H. C. Nguyen, J. Wigard, and P. Mogensen, "Interference Analysis for UAV Connectivity over LTE Using Aerial Radio Measurements," in *2017 IEEE 86th Vehicular Technology Conference (VTC-Fall)*. Toronto, ON: IEEE, Sep. 2017, pp. 1–6.

[6] S. A. A. Shah, T. Meyerhoff, R. Grünheid, G. Bauch, and D. Schupke, "Feasibility of Direct Air to Ground Communication via a Terrestrial 5G Network," in *2024 IEEE Wireless Communications and Networking Conference (WCNC)*, 2024, pp. 1–6.

[7] A. Gürbüz, D. M. Mielke, and M. A. Bellido-Manganell, "On the Application of Beamforming in LDACS," in *2022 Integrated Communication, Navigation and Surveillance Conference (ICNS)*. Dulles, VA, USA: IEEE, Apr. 2022, pp. 1–9.

[8] 3rd Generation Partnership Project (3GPP), "NR and NG-RAN Overall description; Stage-2, section 9.2.3.4, 3GPP TS 38.200 Version 17.7.0," Feb. 2024.

[9] A. Prado, H. Vijayaraghavan, and W. Kellerer, "ECHO: Enhanced Conditional Handover boosted by Trajectory Prediction," in *2021 IEEE Global Communications Conference (GLOBECOM)*. Madrid, Spain: IEEE, Dec. 2021, pp. 01–06.

[10] M. I. Saglam, "Conditional handover for non-terrestrial networks," in *2023 10th International Conference on Wireless Networks and Mobile Communications (WINCOM)*, 2023, pp. 1–5.

[11] Z. Zhang, Z. Jiang, B. Yang, and X. She, "A Beamforming-Based Enhanced Handover Scheme with Adaptive Threshold for 5G Heterogeneous Networks," *Electronics*, vol. 12, no. 19, p. 4131, Oct. 2023.

[12] Cuiling Qi, Zhaoyang Zhang, and Chao Wang, "Handover based on receive beamforming in high mobility cellular communication networks," in *2013 International Conference on Wireless Communications and Signal Processing*. Hangzhou, China: IEEE, Oct. 2013, pp. 1–5.

[13] A. Kose, C. H. Foh, H. Lee, and M. Dianati, "Beam-centric Handover Decision in Dense 5G-mmWave Networks," in *2020 IEEE 31st Annual International Symposium on Personal, Indoor and Mobile Radio Communications*. London, United Kingdom: IEEE, Aug. 2020, pp. 1–6.

[14] E. R. Bastidas-Puga, A. G. Andrade, G. Galaviz, and D. H. Covarrubias, "Handover based on a predictive approach of signal-to-interference-plus-noise ratio for heterogeneous cellular networks," *IET Communications*, vol. 13, no. 6, pp. 672–678, Apr. 2019.

[15] V. Towhidlou, S. Al-Rubaye, and A. Tsourdos, "LTE Handover Design for Cellular-Connected Aircraft," in *2022 IEEE/AIAA 41st Digital Avionics Systems Conference (DASC)*. Portsmouth, VA, USA: IEEE, Sep. 2022, pp. 1–5.

[16] G. L. Stüber, *Principles of Mobile Communication*. Cham: Springer International Publishing, 2017.

[17] R. Sun and D. W. Matolak, "Air–Ground Channel Characterization for Unmanned Aircraft Systems Part II: Hilly and Mountainous Settings," *IEEE Transactions on Vehicular Technology*, vol. 66, no. 3, pp. 1913–1925, Mar. 2017.

[18] D. W. Matolak and R. Sun, "Air–Ground Channel Characterization for Unmanned Aircraft Systems—Part III: The Suburban and Near-Urban Environments," *IEEE Transactions on Vehicular Technology*, vol. 66, no. 8, pp. 6607–6618, Aug. 2017.

[19] 3rd Generation Partnership Project (3GPP), "Physical layer measurements, 3GPP TS 38.215 Version 18.2.0," Mar. 2024.

[20] S. Alraih, R. Nordin, I. Shayea, N. F. Abdullah, and A. Alhammadi, "Ping-Pong Handover Effect Reduction in 5G and Beyond Networks," in *2021 IEEE Microwave Theory and Techniques in Wireless Communications (MTTW)*. Riga, Latvia: IEEE, Oct. 2021, pp. 97–101.

[21] 3rd Generation Partnership Project (3GPP), "Study on channel model for frequencies from 0.5 to 100 GHz, 3GPP TR 38.901 Version 17.0.0," Apr. 2022.

[22] Swiss Federal Office of Communications, "5G Antenna Locations," Feb. 2024. [Online]. Available: http://data.geo.admin.ch/ch.bakom.mobil-antennenstandorte-5g/data/ch.bakom.mobil-antennenstandorte-5g_en.json